Accepted Manuscript

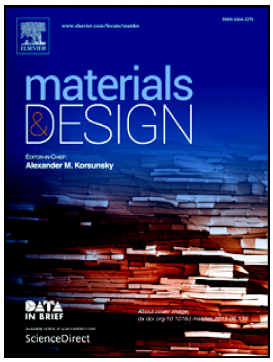

3D printing assisted finite element analysis for optimising the manufacturing parameters of a lumbar fusion cage

Elena Provaggi, Claudio Capelli, Benyamin Rahmani, Gaetano Burriesci, Deepak M. Kalaskar

PII:	S0264-1275(18)30889-X
DOI:	https://doi.org/10.1016/j.matdes.2018.107540
Article Number:	107540
Reference:	JMADE 107540
To appear in:	*Materials & Design*
Received date:	17 September 2018
Revised date:	4 December 2018
Accepted date:	6 December 2018

Please cite this article as: Elena Provaggi, Claudio Capelli, Benyamin Rahmani, Gaetano Burriesci, Deepak M. Kalaskar , 3D printing assisted finite element analysis for optimising the manufacturing parameters of a lumbar fusion cage. Jmade (2018), https://doi.org/10.1016/j.matdes.2018.107540

3D printing assisted finite element analysis for optimising the manufacturing parameters of a lumbar fusion cage

Authors: Elena Provaggi [a,b], Claudio Capelli [c], Benyamin Rahmani [d], Gaetano Burriesci [d,e], Deepak M. Kalaskar [a,b]

[a] *UCL Institute of Orthopaedics and Musculoskeletal Science, Division of Surgery & Interventional Science, University College London (UCL), Brockley Hill, Stanmore, Middlesex HA7 4LP, United Kingdom*

[b] *Centre for Nanotechnology and Regenerative Medicine, Division of Surgery & Interventional Science, University College London (UCL), Rowland Hill Street, London NW3 2PF, United Kingdom*

[C] *Institute of Cardiovascular Science, Great Ormond Street Hospital for Children, University College London (UCL), Great Ormond Street, London WC1N 3JH, United Kingdom*

[d] *Cardiovascular Engineering Laboratory, UCL Mechanical Engineering, University College London, Torrington Place, London WC1E 7JE, United Kingdom*

[e] *Ri.MED Foundation, Bioengineering Group, Palermo 90133, Italy*

Corresponding author:

Correspondence to Deepak M. Kalaskar.

Email: d.kalaskar@ucl.ac.uk

Abstract

The study herein combines the use of fused filament fabrication (FFF) with finite element analysis (FEA) to enhance the understanding of certain manufacturing parameters (i.e. material, infill density, infill pattern, and outer vertical shell) in the design process of a lumbar fusion cage. Three FFF materials with distinct mechanical properties namely polycarbonate (PC), acrylonitrile butadiene styrene (ABS), and polylactic acid (PLA) were tested. Three infill densities (i.e. 25%, 50%, 75%) were investigated along with two different infill patterns (i.e. rectangular and honeycomb). Compressive modulus and compressive yield strength values obtained from standard mechanical analysis were used as input for FEA to assess numerically the mechanical performance of a lumbar fusion cage under physiological static loading. The findings suggest that both infill density and infill pattern influence the quality of the finished part in terms of both printing accuracy and mechanical response. FEA results indicate that both PC and ABS can be safely adopted to fabricate a porous lumbar cage with a 50% honeycomb infill density and a honeycomb infill pattern. This paper demonstrates that 3D printing assisted FEA can be used to predict the performance of a lumbar cage design with varying manufacturing parameters and potentially reduce product design and development time.

Keywords: Fused filament fabrication; Infill density; Infill pattern; Finite element analysis, Medical device, Lumbar cage

Highlights

- Porous structures printed by fused filament fabrication (FFF) with varying material, infill density and infill pattern has been studied.
- Compressive results were used as input for the finite element analysis (FEA) to optimise the manufacturing process of a lumbar fusion cage.
- Honeycomb structures exhibited higher dimensional accuracy and higher compressive properties than rectangular structures, although being related with higher volume fraction.
- Finite element analysis (FEA) allowed the selection of optimal materials and cage structure capable to withstand the maximum static loads expected after implantation.

Graphical abstract

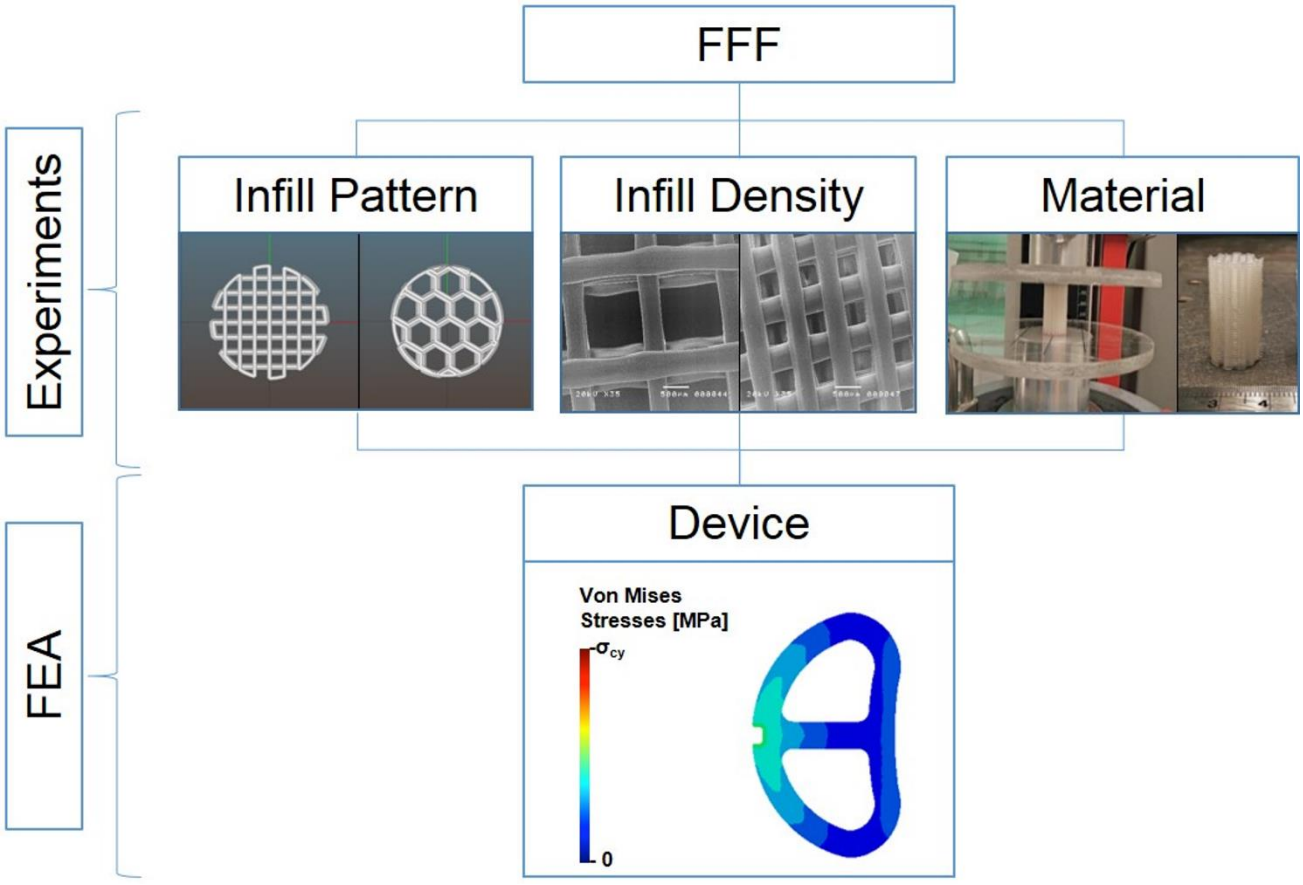

Abbreviations

ABS Acrylonitrile Butadiene Styrene

CAD Computer Aided Design

DSC Differential Scanning Calorimetry

E_c Compressive Modulus

FEA Finite Element Analysis

FFF Fused Filament Fabrication

IVG Intervertebral Disc Degeneration

Ns Number of Shells

PC Polycarbonate

PLA Polylactic Acid

SEM Scanning Electron Microscopy

SLA Stereolitography

σ_{cy} Compressive Yield Strength

µCT Micro-Computed Tomography

1. Introduction

Within the last decade, 3D printing has been increasingly employed in the biomedical industry as an effective technology for rapid prototyping and production of medical devices (1). In most medical fields, low-volume porous structures are developed to tailor the mechanical properties of the host tissue, increase biocompatibility and reduce costs of production, with applications including permanent cellular implants and biodegradable scaffolds for orthopaedics, dentistry and reconstructive surgery (2-4). Accordingly, 3D printing technology can overcome the issues of conventional fabrication approaches and allow for the fabrication of controllable structures with desired porosity, pore size and architecture (5, 6). Within the class of 3D printing technologies, fused filament fabrication (FFF) has the advantage of cost-effectiveness combined with high degree of customisation. This allows the generation of porous objects with varying level of material densities and pattern geometries, the optimisation of designs for low-volume products, and the control of process parameters such as temperature and speed of extrusion (7-9). Additionally, various medical-grade polymers can be processed via FFF for medical device manufacturing. As a permanent solution in spinal surgery, the viability of polycarbonate (PC) fusion cages fabricated via FFF technology has been shown (10, 11), whilst bioresorbable spinal cages made in polylactic acid (PLA) have been investigated for their time-engineered degradation (12, 13). Acrylonitrile butadiene styrene (ABS) has not yet been proposed for manufacturing spinal cages, however, studies on both ABS and PLA scaffolds printed with an inexpensive desktop 3D printer have shown sustained mechanical stability, while demonstrating good cell proliferation and neo-matrix formation for cartilage and nucleus polposus regeneration (14). Medical-grade ABS and PLA have also been used as the building materials for FFF low-cost customised surgical guides and low-weight prosthesis for maxillo-facial and orthopaedic surgery (15-17).

In this context, it becomes critical to understand the influence of chosen manufacturing parameters on the final 3D printed structure. Design parameters such as the internal infill density and pattern have shown to influence the mechanical behaviour of FFF porous parts (18-20). The increase in infill density always entails an increase in tensile and compressive strength (21, 22) and was found to be more effective than the infill pattern to improve the strength of FFF parts (23). Accordingly, ABS parts fabricated with 100% rectangular pattern were found to be related to a higher tensile strength, whilst a stiffer behaviour was found associated to parts fabricated with honeycomb pattern at lower infill (24). Indeed, honeycomb structures have been shown to facilitate the load transfer between layers, thus providing higher mechanical strength, failure reliability and fatigue resistance (25).

Because of the large variability of manufacturing parameters, the integration of simulation tools like finite element analysis (FEA) with FFF is particularly attractive to design 3D printed products and analyse the mechanics of complex geometries. FEA has the remarkable strength to accelerate product design and development process; however, the complexity and variability of 3D printing brings the risk of simplified assumptions that can lead to inaccurate solutions (26). Accordingly, there are attempts to combine these two technologies to facilitate the understanding of certain process parameters and predict the mechanical strength of 3D printed parts (27-29). This combined approach has demonstrated to be an efficient tool to test partially porous 3D printed titanium cages with various architectures, both numerically and experimentally (30, 31).

Hence, the aim of this study is twofold. First, we aimed to investigate the effect of material, infill density and infill pattern on the printing accuracy, repeatability and mechanical properties of FFF 3D printed structures. Secondly, by means of FEA, we aimed

to select the optimal materials and cage structure capable to withstand the maximum static loads expected after implantation.

2. Materials and methods

2.1 Materials and design

Three filament materials were selected for the fabrication of porous structures using fused filament fabrication (FFF): PC (Gizmo Dorks, USA, 1.75mm, Blue); ABS (Orbi-Tech, Germany, 1.75mm, Blue); and, PLA (3Dison, Korea, 1.75mm, Natural). Samples for compression testing were designed based on the ASTM D-695 (cylindrical shape, 12.7 mm diameter, 25.4 mm height) (32). STL files of the specimen were imported into an open-source slicing software (Slic3r 1.2.9) to define manufacturing parameters. Three infill densities (i.e. 25%, 50% and 75%) and two pattern geometries (i.e. rectangular and honeycomb) were considered. Accordingly, six designs were generated per each material based on each combination of infill density and pattern geometry. Moreover, a solid design with 100% rectangular infill was included as control group.

2.2 Sample fabrication

Commercially available desktop FFF printer (FLASHFORGE Dreamer Dual Extrusion 3D Printer, USA) was employed to build the specimens. The printer was standardly equipped with a nozzle of 0.4 mm diameter. The printing parameters adopted in this study are shown in Table I. Processing parameters such as extruding temperature, bed temperature and infill speed were calibrated to achieve a uniform layer height of 0.3 mm. Test samples were manufactured with each combination of material and infill design for a total of 18 groups of study and 3 control groups containing 9 samples each.

Material	Layer height	Infill speed	Travel speed	Extrusion	Bed temperature

	(mm)	(mm s^{-1})	(mm s^{-1})	temperature (°C)	(°C)
PC	0.3	60	60	265	100
ABS	0.3	30	60	230	70
PLA	0.3	15	60	185	50

Table I. Printing parameters used for each polymer during the FFF process. The infill speed corresponds to the speed to which the infill material is extruded, whilst the travel speed is the speed of the printing head while not extruding.

2.4 Printing accuracy and repeatability

Scanning electron microscopy (Philips FEI 501) was used to inspect the surface topographies of the FFF 3D printed porous structures. Samples were sputter coated with 20 nm of gold using a Quorum Q150RS instrument prior to examination.

The dimensions (i.e. diameter, height) of the fabricated structures were measured using a digital caliper (Schut Geometrical Metrology, 0–25 mm measurement range, 0.001 mm accuracy). As a measure of dimensional accuracy, the dimensional difference (%) between the measured linear dimensions and the nominal corresponding values of the cylindrical CAD design were calculated for each sample (N=3 specimens per group). The standard deviations of the measured linear dimensions were taken as a measure of repeatability.

The internal volume fraction of the printed FFF structures was quantitatively evaluated through micro-computed tomography (μCT) by using a high-resolution scanner Sky-Scan1174 (Bruker). Images were acquired using a voxel size of 11.31 μm, an applied voltage of 40 kV, a current of 250 μA, an exposure time of 146 ms, a rotation step of 0.6 deg, no metal filter, and no frame averaging. Three samples per group were scanned with identical acquisition parameters. NRecon software (SkyScan, Bruker) was used to reconstruct cross-section images from the acquired tomography projection images. The cross-section images were imported into Simpleware ScanIP (Synopsys, Mountain View,

USA) for post-processing and quantitative analysis. All images were re-sampled at a pixel spacing of 0.05 x 0.05 x 0.02 mm. The 3D background volume was treated with a median filter (1 px radius) and a thresholding algorithm (range 40-255) before generating the segmented mask. A mask statistics template was created for measuring the voxel volume fraction (%) of the mask within a previously defined region of interest (ROI) of sample size. As a measure of volume fraction accuracy, the difference (%) between the experimental volume fraction measurement and the nominal infill density of a given structure was calculated. The standard deviations of the volume fraction measurements were taken as a measure of repeatability.

2.5 Mechanical characterisation

Compressive tests on the fabricated samples were performed according to the ASTM D695 (32). Tests were conducted using a Zwick Roell testing machine BT1-FR5 equipped with a 5 kN load cell (Zwick Roell, GmbH, Germany), operated in displacement control setting a displacement rate of 1 mm/min. The maximum displacement was set at 2.54 mm, equivalent to the 10% of the initial length. No preload was applied. The specimens were positioned according to their building direction and loaded parallel to the pore orientation (Figure 1). A total of 126 samples were tested (i.e. N=6 specimens per group). Experimental data were analysed with Matlab (MATLAB 2014a, The MathWorks Inc.) to derive the compressive modulus (E_c) and compressive yield strength (σ_{cy}). A toe compensation algorithm was implemented to remove the superficial artefact attributable to the specimen roughness and apply a zero-strain correction. Stress corresponding to the applied force was calculated based on the nominal cross-sectional area of the cylindrical specimens (126.7 cm^2).

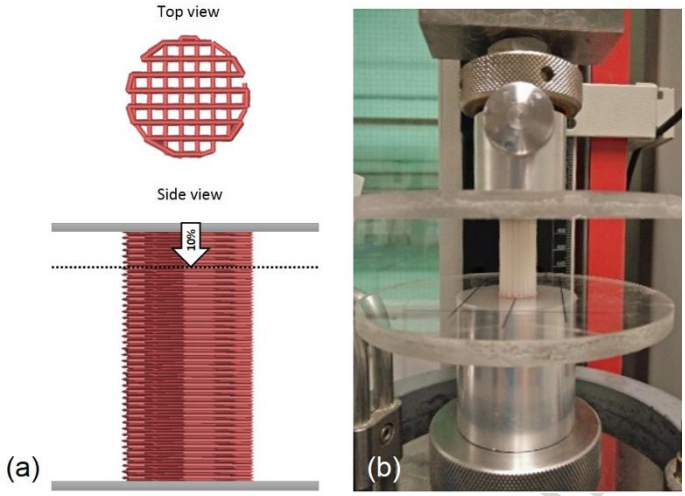

Figure 1. Visualization of the experimental set up: (a) Diagram and (b) picture of the compressive testing equipment and sample.

2.6 FEA of 3D printed cage

The CAD design of an anatomically shaped cage for anterior lumbar interbody fusion (ALIF) was tested in this part of the study (10). FEA was performed to optimise manufacturing parameters of the cage and select the optimal structure capable to withstand the maximum expected loads with the minimum material and manufacturing time. Specifically, infill density, infill pattern and the inclusion of an outer vertical shell were investigated. In particular, the outer vertical shell was included in the design development process to investigate its effect on cage mechanical stability, whilst allowing vertical bone ingrowth through the exposure of the inner porous structure (Figure 2). The number of shells (Ns) was varied from 0 to 3, by changing the thickness of the outer solid shell from 0.3 (Ns=1) to 0.9 mm (Ns=3). Mechanical properties of both solid and porous polymers were assumed to be homogeneous isotropic and linear elastic. The porous material was modelled as a continuum using the experimental apparent-level compressive modulus (E_c) obtained for the different materials (PC, ABS, PLA), and combinations of infill densities (25%, 50%, 75%) and pattern geometries (rectangular and honeycomb). The outer vertical

shell was modelled using the experimental compressive modulus obtained for the 100% rectangular control group. The cage was meshed using linear solid tetrahedron elements (C3D4) for the porous infill and linear shell triangular elements (S3) for the outer shell. Element approximate global size was set at 1 mm following a sensitivity analysis from a previous study from our group (10). Top and bottom surfaces of the cage were tied to two compression plates modelled as rigid bodies. The compression plates were meshed with linear shell triangular elements (S3). FEA was performed in two subsequent steps: 1) a compressive axial load of 1,000 N was applied to the centre of mass of the top compression plate to simulate the load corresponding to a standing position; 2) a moment of 15 Nm was applied to the centre of mass of the top compression plate with varying direction to simulate independently the physiological loading conditions of flexion, extension, torsion and lateral bending.(33) The bottom plate was constrained with an encastre boundary condition. Resulting maximum Von Mises stresses in the porous component of the model were compared to the compressive yield strength (σ_{cy}) values obtained experimentally for the different combinations of infills. FEA results highlighted the optimal infill condition defined as the lowest amount of material theoretically used, whilst assuring sufficient mechanical strength.

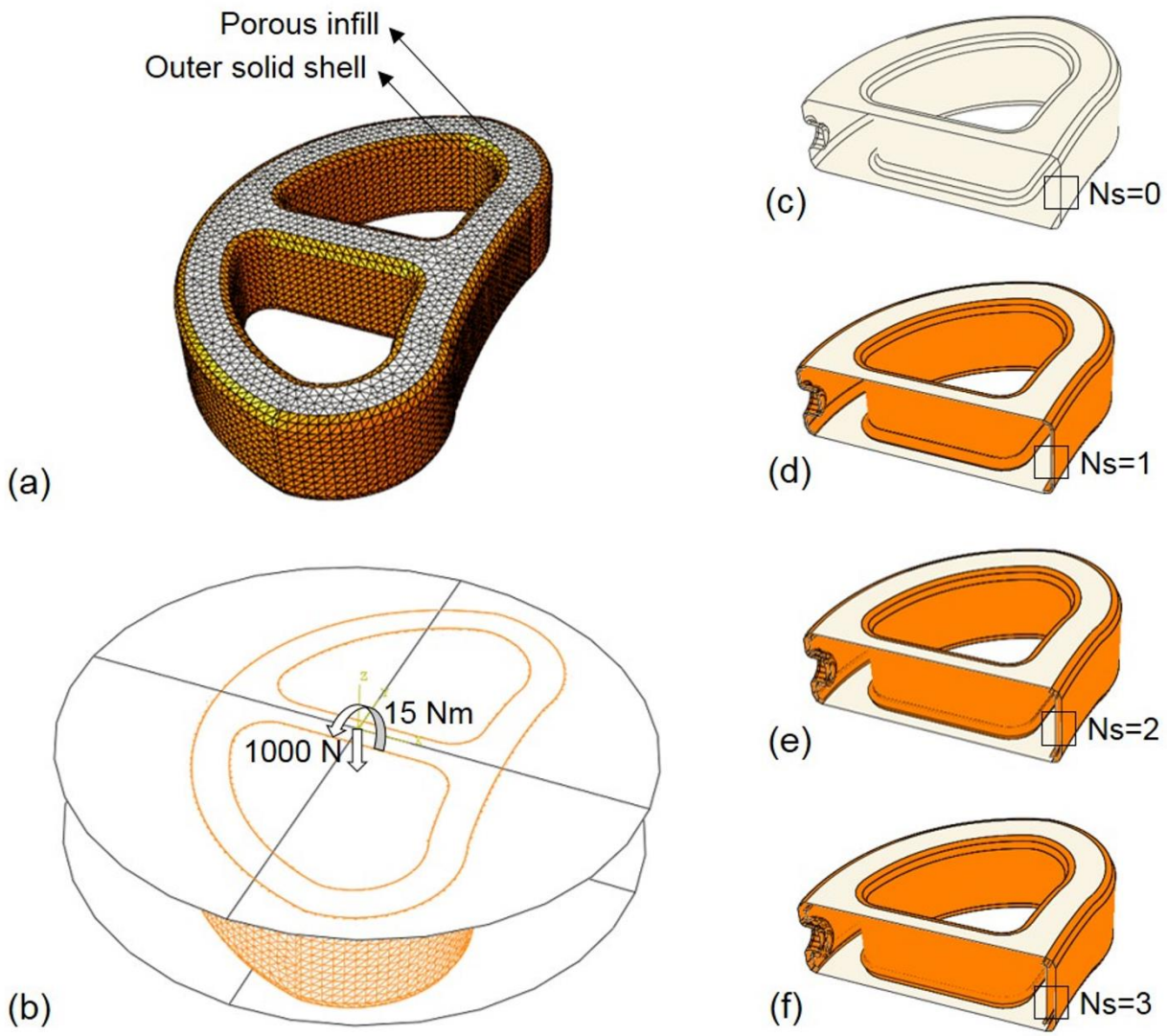

Figure 2. Model of the porous spinal fusion cage used in this study (a) and diagram of the loading conditions (b). The effect of the number of outer vertical shells on mechanical behaviour was investigated by varying Ns (c-f).

2.7 Statistical analysis

All the results are here reported as means ± standard deviation (SD). Statistical analysis was performed using GraphPad Prism 6.0 (GraphPad Software Inc.) applying unpaired T-test or two-way analysis of variance (ANOVA) and Tukey's multiple comparison test. P-values below 0.05 were considered significant.

3. Results and discussion

3.1 Printing accuracy and repeatability

SEM and μCT reconstructions (Figure 3) reveal the architecture and pore size of the 3D porous structures fabricated using the different materials. The increase in infill density, which corresponds to a decrease in porosity, also entailed a reduction in pore size. The pore size of a structure with a given infill density was observed to be larger for the honeycomb pattern than for the rectangular pattern (Figure 3). This mismatch in pore size between patterns was found to be inherent to the infill design generated by the slicing software (i.e. Slic3r) (34). It is also noticeable that, at high infill density, the geometry of the honeycomb pores was poorly distinguishable. The higher the infill density, the more the deposited fibers resemble straight lines. Also, the slicing software did not generate a full 100% infill with honeycomb pattern. This effect was due likely to the way the porous geometry is generated. In the rectilinear pattern, rectangular pores are generated by depositing one linear layer over another at 90° angle variation. Hence, this deposition produces well defined rectangular pores with sharp edges. In the honeycomb structures, instead, hexagonal pores are generated at every single layer; thus, the poor positional accuracy causes round-edged hexagonal pores. Additionally, PC honeycomb samples with 75% infill density exhibited a structure with higher apparent density compared to the equivalent samples fabricated in ABS and PLA. This shows a material-specific variability of printing quality.

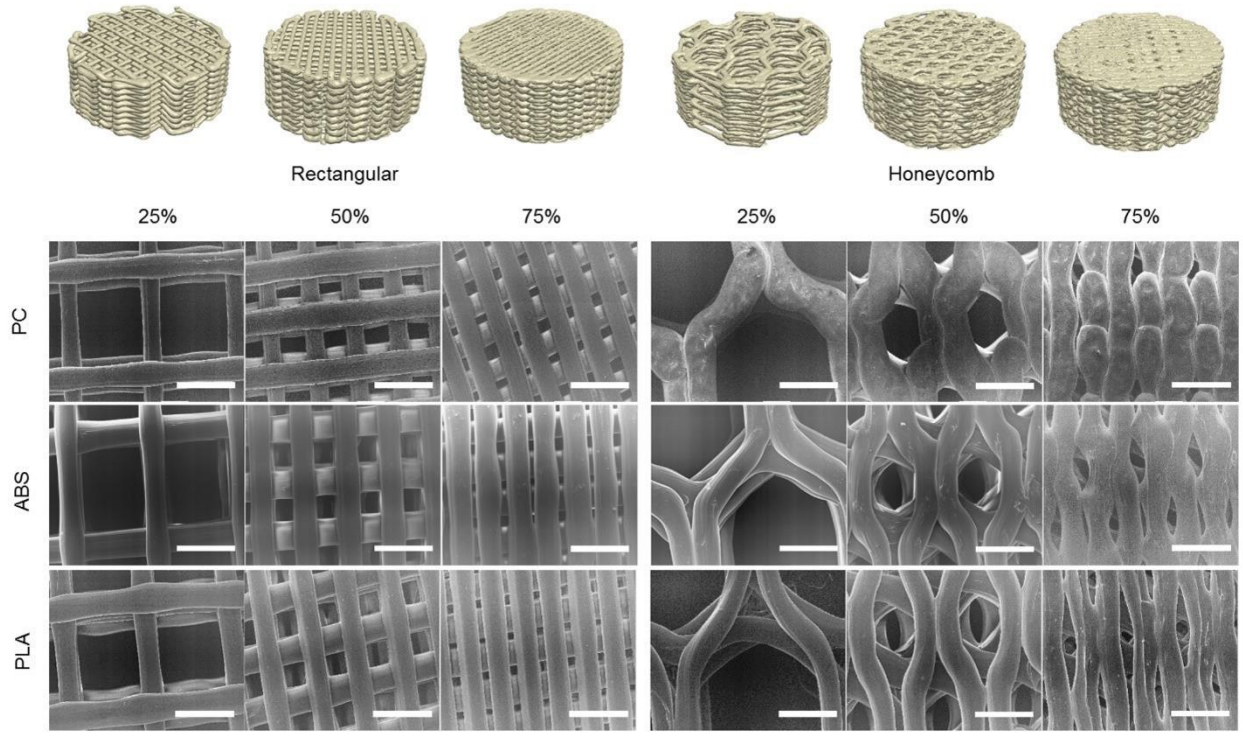

Figure 3. Internal architectures of the 3D porous structures. SEM revealing pore size and infill architecture of the rectangular and honeycomb patterns for all the set of studied materials (Scale bars: 1 mm). µCT-based 3D reconstructions, displayed as a reference for PC (top), show structure geometry and porosity analogous to the SEM images of the same structure.

The external dimensions (i.e. diameter, height) of the printed structures are reported in Figure 4. Overall, both diameter and height of all printed samples were found to be material-dependent. Also, for a given infill density, differences in dimensional accuracy were found between patterns. PC samples printed with rectangular pattern had greater diameter ($p<0.001$) and entailed lower dimensional accuracy (≤ 3.37 %). On the contrary, parts printed in PC with honeycomb pattern exhibited higher dimensional accuracy (≤ 0.90 %). Parts fabricated in PLA had the least diameter and height measurements, with no significant differences between patterns, thus showing lower dimensional accuracy compared to PC or ABS. Overall, low standard deviation for sample dimensions

demonstrated high dimensional repeatability. Results of statistical analysis of external dimensions including statistical differences between infill densities and theoretical values are reported as additional information (Table A.1-A.6).

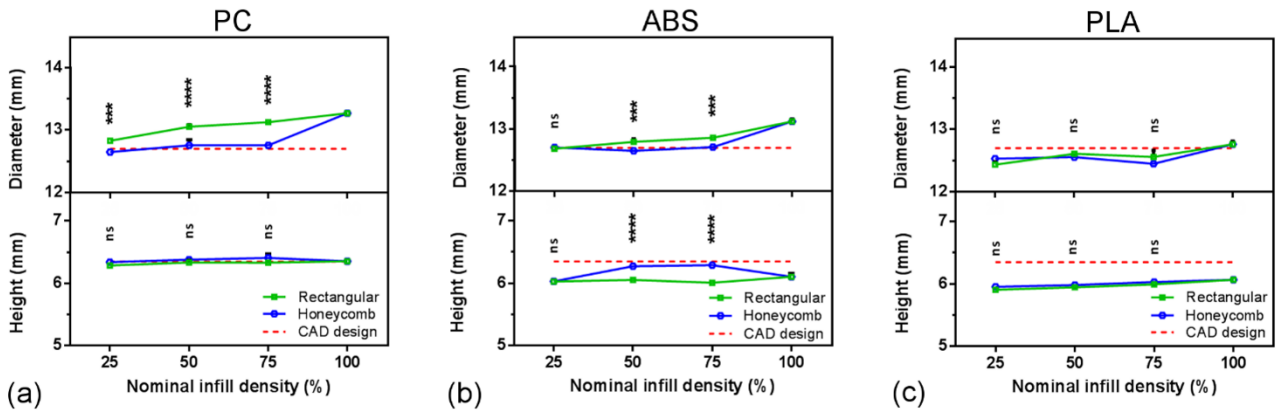

Figure 4. External linear dimensions of all FFF porous structures. Measurements are shown for structures fabricated in (a) PC; (b) ABS; and (c) PLA (means ± SD, N=3). The dimensional accuracy was linked with the dimensional difference calculated based on the nominal dimensions of the CAD design (red dashed line). P-values (2-way ANOVA) represent correlation coefficients between patterns (* significant at $p<0.05$; ** significant at $p<0.005$; *** significant at $p<0.001$; **** significant at $p<0.0001$; ns not significant at $p\geq0.05$).

Figure 5 shows the µCT-based volume fraction measurements of the printed structures as a function of their nominal infill density. The highest volume fraction accuracy was measured with rectangular infill (< 5.2%). Samples printed with honeycomb pattern showed significantly higher values of volume fraction compared to both the theoretical values ($p<0.0076$) and the measured values of the samples printed with rectangular pattern ($p<0.01$). This discrepancy in volume fraction was found to be associated with a greater amount of material needed for printing with honeycomb pattern. This excess deposition of material might be related to instabilities in the extrusion flow inherent to the pattern geometry as well as to the estimation of the amount of material required for printing the part as calculated by the slicing software (i.e. Slic3r).(35) Accordingly, Table II highlights that the

amount of material estimated by Slic3r is different between patterns with equal infill density. In respect to the internal porous structure, small standard deviation for volume fraction values evidenced satisfactory printing repeatability. Results of statistical analysis including statistical differences with theoretical values of infill density are reported as additional information (Table A.7-A.9). Control samples fabricated at 100% infill density were not found to be 100% solid as theoretically expected. This has been previously linked with the presence of gaps, caused by the layer-by-layer deposition of extruded material during the FFF process.(36)

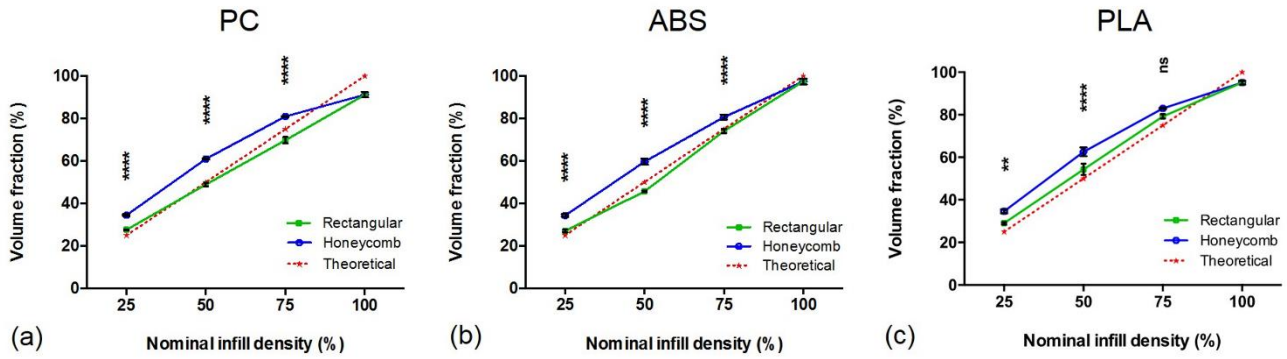

Figure 5. µCT-based volume fraction results of the FFF porous structures. Measurements are shown for structures fabricated in (a) PC; (b) ABS; and (c) PLA (means ± SD, N=3). The internal volume fraction accuracy was linked with the volume fraction difference between the printed object and the theoretical value of infill density. P-values (2-way ANOVA) represent correlation coefficients between patterns (* significant at $p<0.05$; ** significant at $p<0.005$; *** significant at $p<0.001$; **** significant at $p<0.0001$; ns not significant at $p\geq0.05$).

	Rectangular pattern		Honeycomb pattern	
Nominal infill density (%)	**Estimated printing time (min)**	**Estimated material needed (m)**	**Estimated printing time (min)**	**Estimated material needed (m)**

25	7	0.42	8	0.51
50	7	0.74	8	0.84
75	8	1.05	10	1.12
100	8	1.39	N/A	N/A

Table II. Estimated printing time and material needed for a given infill density and pattern for the fabrication of a test specimen. Estimated values were obtained from Slic3r.

3.2 Mechanical characterisation

The compressive modulus (E_c) and compressive yield strength (σ_{cy}) values, corresponding to the nominal cross-sectional area of the samples, are shown in Figure 6. Both E_c and σ_{cy} were found to increase in a linear fashion as the infill density increased, as indicated by the R^2 values plotted for each pattern (Figure 6). Overall, structures printed with honeycomb pattern at a given nominal infill density exhibited higher E_c and σ_{cy} values than structures printed with rectangular pattern. The higher mechanical properties of the honeycomb pattern might be associated with the higher values of volume fraction. Hence, selecting the appropriate infill pattern during the slicing stage could provide an effective tool to alter and predict the mechanical behaviour of 3D printed porous structures. Importantly, for all the studied materials, the compressive modulus values at 100% nominal infill were found to be lower than the values reported in literature for the respective filament materials (37-39). This finding might be explained as a direct consequence of the FFF technology, for several reasons. First, our study highlighted that the FFF process generates gaps within the solid material, confirming the inherent limitations of the manufacturing process (18). A decrease of 11% to 37% in modulus and 22% to 57% in strength has been reported for FFF printed ABS parts when compared with the respective ABS source filament, which has been linked with the presence of voids (40). Secondly, because of the layer-by-layer deposition, the anisotropy of the layered structure increases. Accordingly, the compressive modulus is likely to be different based on the testing direction (41, 42). Lastly, for semi-

crystalline polymers (e.g. PLA), several printing parameters such as extrusion temperature and bed temperature have been shown to induce an effect on the crystallinity fraction (Xc), thus influencing the material mechanical properties (36).

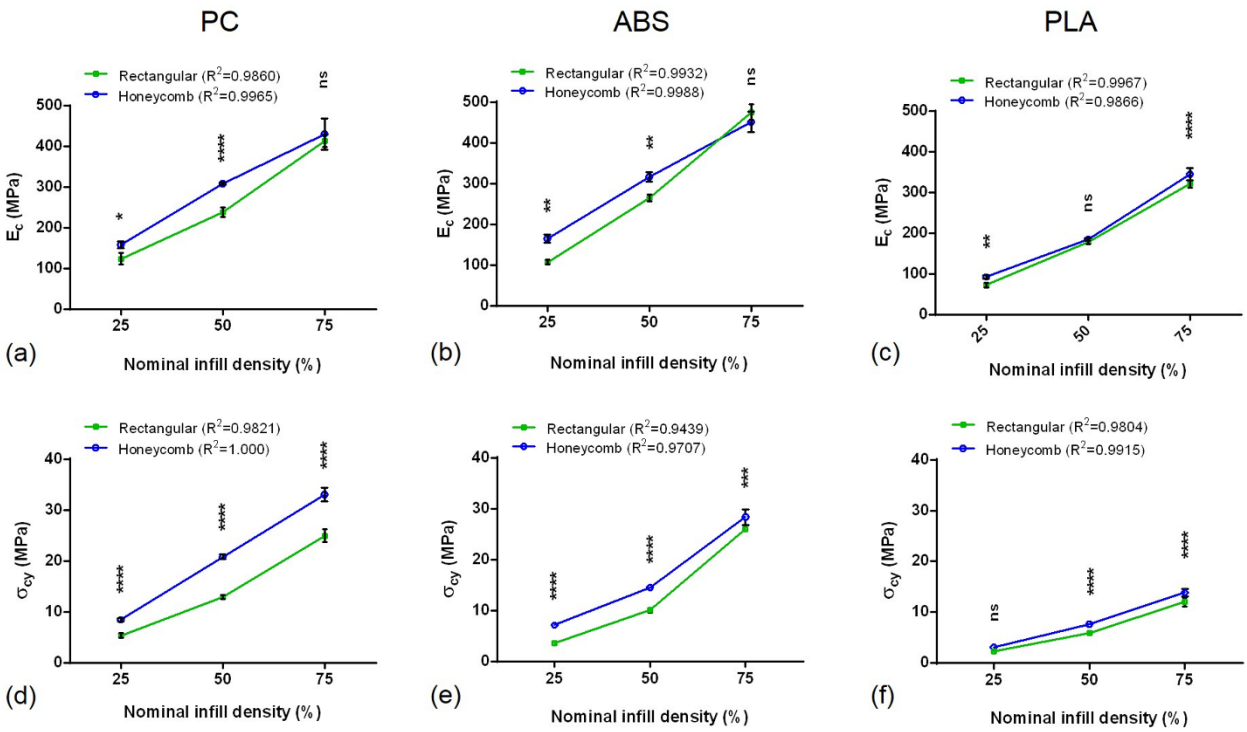

Figure 6. Mechanical properties of the FFF porous structures. The compressive modulus (E_c) are and compressive yield strength (σ_{cy}) values are shown as a function of the nominal infill density for PC (a,d); ABS (b,e); and, PLA (c,f) structures. The R^2 values corresponding to each linear regression line are plotted for each pattern (n=6). P-values (2-way ANOVA) represent correlation coefficients between patterns (* significant at $p<0.05$; ** significant at $p<0.005$; *** significant at $p<0.001$; **** significant at $p<0.0001$; ns not significant at $p\geq0.05$).

Compressive modulus values of the tested materials fell within the range of trabecular bone values (1-9800 MPa) (43). Previous studies have shown that the Young's modulus of trabecular bone is dependent on the anatomical location, thus different results have been found for vertebral, femural, tibial, or mandibular bone (44, 45). Trabecular bone samples obtained from vertebral anatomical sites have been found to be related with the

lowest compressive modulus (329 MPa) and compressive yield strength (1.62 MPa) when compared with proximal tibial and femoral neck sites (46). Accordingly, the mechanical properties of FFF low-volume implants or porous scaffolds can be potentially tailored based on both parameters of infill density and infill pattern to achieve the optimal mechanical stability required for the implantable site. Positively, compressive yield strength results of all combinations of materials and infills tested in this study were found to be higher than the compressive yield strength of human vertebral trabecular bone (1.62 MPa) (46).

3.3 FEA of 3D printed cage

Maximum Von Mises stresses (14.25 MPa) were obtained under the combination of a compressive load with a flexion moment, in accordance with previous experimental and numerical studies on the lumbar spine (47). Accordingly, this loading condition was adopted as the most critical scenario for all analysis. The maximum Von Mises stresses obtained for all combinations of materials, infills and Ns were compared with the respective values of experimental compressive yield strength (Table III). Stresses in the inner porous part of the cage decreased with increasing Ns (Figure 6). Therefore, combining an outer vertical solid shell with a low-density inner infill improved the mechanical strength of the cage by reducing high stress concentrations that could lead to implant failure. Based on our results, cages printed with any of the tested materials at 25% infill and Ns ≤ 3 were not capable of withstanding the maximum expected static loads. A thicker solid wall (Ns > 3) may benefit to further reduce the maximum stresses on the porous component, although this has been related with higher amount of material used. The optimal infill conditions which assured sufficient mechanical strength and minimum material consumption whilst potentially allowing bone ingrowth through the internal porous structure, were 50% infill density, honeycomb infill pattern, and Ns = 0. This condition, achievable by using PC or ABS as the

building material, was related to the lower estimation of material (0.49 m) and printing time (7 min). It is important to highlight that the infill density was taken as a discrete variable, thus the optimal infill condition was determined based on the three conditions of infill design considered in this study. Hence, considering the infill density as a continuous variable may generate a different optimal infill condition.

		PC		ABS		PLA	
Infill	**Ns**	**Maximum Von Mises stress (MPa)**	**Compressive yield strength (MPa)**	**Maximum Von Mises stress (MPa)**	**Compressive yield strength (MPa)**	**Maximum Von Mises stress (MPa)**	**Compressive yield strength (MPa)**
R 25	0	13.72	5.39 ± 0.44	13.73	3.62 ± 0.12	13.8	2.30 ± 0.14
	1	12.37		12.07		12.53	
	2	9.46		8.45		9.1	
	3	7.46		6.32		6.65	
H 25	0	13.63	8.47 ± 0.36	13.72	7.14 ± 0.28	14.25	3.08 ± 0.14
	1	12.71		12.88		12.66	
	2	10.46		10.05		9.56	
	3	8.43		7.71		7.27	
R 50	0	13.76	12.89 ± 0.41	13.67	10.09 ± 0.43	14.12	5.96 ± 0.32
	1	12.77		12.47		13.22	
	2	10.76		10.45		11.2	
	3	9.11		8.83		9.36	
H 50	0	13.6	20.86 ± 0.53	13.61	14.56 ± 0.26	14.15	7.62 ± 0.26
	1	12.77		12.8		13.28	
	2	11.19		11.02		11.31	
	3	9.79		9.34		9.44	
R 75	0	13.4	24.97 ± 1.24	13.69	25.79 ± 0	13.6	12.01 ± 0.92
	1	12.71		12.95		12.93	
	2	11.4		11.49		11.53	
	3	10.27		10.27		10.33	
H 75	0	13.47	33.07 ± 1.31	13.5	28.37 ± 1.54	13.5	13.89 ± 0.77
	1	12.78		12.72		13	
	2	11.48		11.33		11.76	
	3	10.33		10.08		10.48	

Table III. Maximum Von Mises stresses (MPa) calculated on the internal porous area of the lumbar cage with varying materials, infills and Ns. Maximum Von Mises stresses (MPa) higher than the respective compressive yield strength values are considered unsafe (red values) as could lead to implant failure. Green values indicate safe conditions.

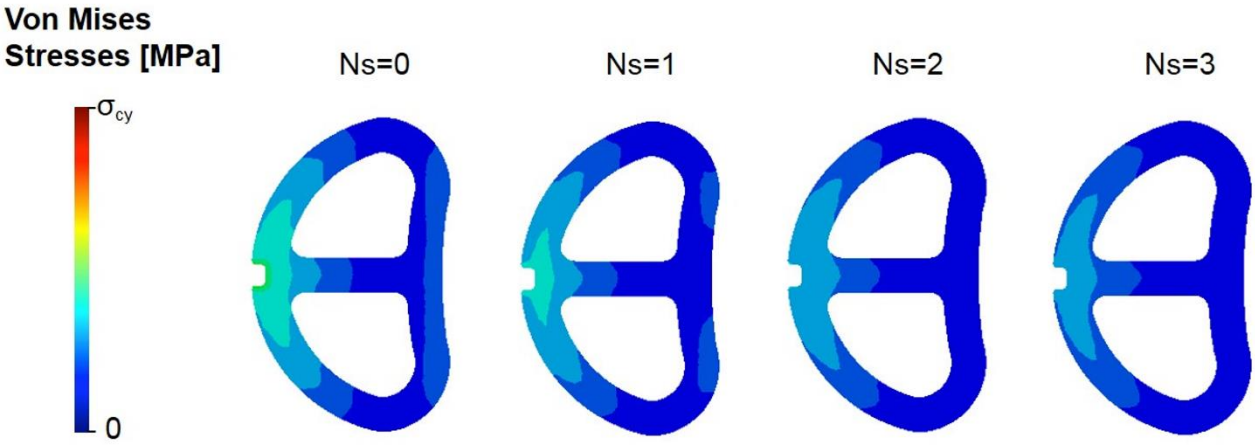

Figure 7. Von Mises stress distributions at the cross-section of the lumbar cage printed in PC with honeycomb infill pattern at 50% infill density (H 50), with varying Ns. The maximum value of the scale corresponds to the experimental compressive yield strength (σ_{cy}) value obtained from the mechanical analysis of the respective printed structures (H 50). Stress concentrations higher than the respective compressive yield strength values are considered unsafe as could lead to implant failure.

The FE model used in this study presented some limitations. First, the porosity of the model was not taken into account from a geometrical point of view. This simplification did not allow to gather information on potential stress concentrations of the micro-structure. Secondly, the material properties of the different components were assumed to be linear elastic, which may overestimate the mechanical strength of the cage. In addition to this, evaluating the anisotropic mechanical properties of the layered structures would allow for an anisotropic finite element formulation which will further increase the reliability of the results. Lastly, fatigue testing would be recommendable to predict longer term response of such a device. Additionally, further testing could take into account combined moments of multiple physiological loading conditions of flexion, extension, torsion and lateral bending. Our results were indicative of the specific FFF printer chosen in this study and the selected slicing software. Hence, using a different FFF equipment or designing similar pattern geometries with a different software could produce different results. Additionally, in setting the printing parameters, we were only able to control the layer height and not the layer width. Advanced research should be focused on assessing the influence of residual

stresses, thermal conductivity and polymer mechanical properties on the shape changes observed in the printed structures. Nevertheless, this study highlights the influence of FFF parameters which need to be taken into account when this technology is used to manufacture a medical device.

4 Conclusions

In this study, we combined the use of FFF 3D printing with FEA to enhance the understanding of certain manufacturing parameters (i.e. material, infill density, infill pattern, and outer vertical shell) in the design process of a lumbar fusion cage. Accordingly, the printing accuracy, repeatability and mechanical behaviour of porous 3D printed structures were investigated, and the experimental compressive modulus values were used as input for the FEA. Overall, the porous structures fabricated with honeycomb pattern exhibited higher dimensional accuracy and higher compressive properties than rectangular structures, although being related with higher volume fraction. 3D printing assisted FEA was used to verify the performance of the cage design with varying manufacturing parameters and potentially reduce product design and development time. Our results indicated that both PC and ABS can be adopted to fabricate a porous cage with a 50% infill density and a honeycomb infill pattern, without the need of a vertical outer solid shell. The combined approach of 3D printing and FEA proposed in this study can be implemented to other 3D printing technologies and materials and applied to the design process of customised load-bearing implants and low-cost surgical guides.

Acknowledgments

This study was supported through a SLMS IMPACT Studentship Funding in conjunction with Ceramisys Ltd. at University College London (Award No. 170401). Authors would like

to gratefully acknowledge Ceramisys Ltd for their support and expertise throughout this project. The authors also thank Professor Timothy Arnett for the usage of the µCT equipment and Anna Worsley for her involvement in the fabrication of the ABS samples.

References

1. Diment LE, Thompson MS, Bergmann JHM. Clinical efficacy and effectiveness of 3D printing: a systematic review. BMJ Open. 2017;7(12).
2. Yanez A, Cuadrado A, Martel O, Afonso H, Monopoli D. Gyroid porous titanium structures: A versatile solution to be used as scaffolds in bone defect reconstruction. Materials & Design. 2018;140:21-9.
3. Zhang BQ, Pei X, Zhou CC, Fan YJ, Jiang Q, Ronca A, et al. The biomimetic design and 3D printing of customized mechanical properties porous Ti6Al4V scaffold for load-bearing bone reconstruction. Materials & Design. 2018;152:30-9.
4. Zhang YS, Yue K, Aleman J, Moghaddam KM, Bakht SM, Yang J, et al. 3D Bioprinting for Tissue and Organ Fabrication. Annals of biomedical engineering. 2017;45(1):148-63.
5. Xu T, Zhao W, Zhu J-M, Albanna MZ, Yoo JJ, Atala A. Complex heterogeneous tissue constructs containing multiple cell types prepared by inkjet printing technology. Biomaterials. 2013;34(1):130-9.
6. Kalita SJ, Bose S, Hosick HL, Bandyopadhyay A. Development of controlled porosity polymer-ceramic composite scaffolds via fused deposition modeling. Materials Science and Engineering: C. 2003;23(5):611-20.
7. Lanzotti A, Grasso M, Staiano G, Martorelli M. The impact of process parameters on mechanical properties of parts fabricated in PLA with an open-source 3-D printer. Rapid Prototyping Journal. 2015;21(5):604-17.
8. Allen RJA, Trask RS. An experimental demonstration of effective Curved Layer Fused Filament Fabrication utilising a parallel deposition robot. Additive Manufacturing. 2015;8:78-87.
9. Ertay DS, Yuen A, Altintas Y. SYNCHRONIZED MATERIAL DEPOSITION RATE CONTROL WITH PATH VELOCITY ON FUSED DEPOSITION MACHINES. Additive Manufacturing. 2017.
10. Serra T, Capelli C, Toumpaniari R, Orriss IR, Leong JJ, Dalgarno K, et al. Design and fabrication of 3D-printed anatomically shaped lumbar cage for intervertebral disc (IVD) degeneration treatment. Biofabrication. 2016;8(3):035001.
11. Figueroa-Cavazos JO, Flores-Villalba E, Diaz-Elizondo JA, Martínez-Romero O, Rodríguez CA, Siller HR. Design Concepts of Polycarbonate-Based Intervertebral Lumbar Cages: Finite Element Analysis and Compression Testing. Applied Bionics and Biomechanics. 2016;2016:7149182.
12. Wuisman PIJM, Smit TH. Bioresorbable polymers: heading for a new generation of spinal cages. European Spine Journal. 2006;15(2):133-48.
13. Cao L, Chen Q, Jiang LB, Yin XF, Bian C, Wang HR, et al. Bioabsorbable self-retaining PLA/nano-sized beta-TCP cervical spine interbody fusion cage in goat models: an in vivo study. International journal of nanomedicine. 2017;12:7197-205.
14. Rosenzweig D, Carelli E, Steffen T, Jarzem P, Haglund L. 3D-Printed ABS and PLA Scaffolds for Cartilage and Nucleus Pulposus Tissue Regeneration. International Journal of Molecular Sciences. 2015;16(7):15118.
15. Dahake Sandeep W, Kuthe Abhaykumar M, Chawla J, Mawale Mahesh B. Rapid prototyping assisted fabrication of customized surgical guides in mandibular distraction osteogenesis: a case report. Rapid Prototyping Journal. 2017;23(3):602-10.
16. McAllister P, Watson M, Burke E. A Cost-Effective, In-House, Positioning and Cutting Guide System for Orthognathic Surgery. Journal of Maxillofacial and Oral Surgery. 2018;17(1):112-4.
17. Fantini M, Crescenzio FD, Ciocca L, Persiani F. Additive manufacturing to assist prosthetically guided bone regeneration of atrophic maxillary arches. Rapid Prototyping Journal. 2015;21(6):705-15.

18. Melenka GW, Schofield JS, Dawson MR, Carey JP. Evaluation of dimensional accuracy and material properties of the MakerBot 3D desktop printer. Rapid Prototyping Journal. 2015;21(5):618-27.
19. Shahrain M, A.J. Q, Lim GK, Didier T. Tensile strength of partially filled FFF printed parts: meta modelling. Rapid Prototyping Journal. 2017;23(3):524-33.
20. Tanikella NG, Wittbrodt B, Pearce JM. Tensile strength of commercial polymer materials for fused filament fabrication 3D printing. Additive Manufacturing. 2017;15:40-7.
21. Sharma R, Singh R, Penna R, Fraternali F. Investigations for mechanical properties of Hap, PVC and PP based 3D porous structures obtained through biocompatible FDM filaments. Composites Part B: Engineering. 2018;132:237-43.
22. Gautam Tanikella N, Wittbrodt B, Pearce J. Tensile Strength of Commercial Polymer Materials for Fused Filament Fabrication 3D Printing2017.
23. Al CM, Yaman U. Improving the strength of additively manufactured objects via modified interior structure. AIP Conference Proceedings. 2017;1896(1):040003.
24. Fernandez-Vicente M, Calle W, Ferrandiz S, Conejero A. Effect of Infill Parameters on Tensile Mechanical Behavior in Desktop 3D Printing. 3D Printing and Additive Manufacturing. 2016;3(3):183-92.
25. Roohani-Esfahani S-I, Newman P, Zreiqat H. Design and fabrication of 3D printed scaffolds with a mechanical strength comparable to cortical bone to repair large bone defects. Scientific reports. 2016;6:19468.
26. Morrison SKaA. Fea and 3D Printing, the Perfect Match? International Journal of Mechanical Systems Engineering. 2016:2: 111.
27. Dalia C, Rimantas B, Daiva M, Rytis M, Audrius N, Armantas O, et al. Multi-scale finite element modeling of 3D printed structures subjected to mechanical loads. Rapid Prototyping Journal. 2018;24(1):177-87.
28. Kantaros A, Chatzidai N, Karalekas D. 3D printing-assisted design of scaffold structures. The International Journal of Advanced Manufacturing Technology. 2016;82(1):559-71.
29. Mahshid R, Hansen HN, Hojbjerre KL. Strength analysis and modeling of cellular lattice structures manufactured using selective laser melting for tooling applications. Materials & Design. 2016;104:276-83.
30. Zhang Z, Li H, Fogel GR, Liao Z, Li Y, Liu W. Biomechanical Analysis of Porous Additive Manufactured Cages for Lateral Lumbar Interbody Fusion: A Finite Element Analysis. World neurosurgery. 2018;111:e581-e91.
31. Tsai PI, Hsu CC, Chen SY, Wu TH, Huang CC. Biomechanical investigation into the structural design of porous additive manufactured cages using numerical and experimental approaches. Computers in biology and medicine. 2016;76:14-23.
32. International A. ASTM D965 - Standard Test Method for Compressive Properties of Rigid Plastics. ASTM International; 2015.
33. Noailly J, Lacroix D Fau - Planell JA, Planell JA. Finite element study of a novel intervertebral disc substitute. Spine. 2005(1528-1159 (Electronic)).
34. Tsai KJ, Dixon S, Hale LR, Darbyshire A, Martin D, de Mel A. Biomimetic heterogenous elastic tissue development. npj Regenerative Medicine. 2017;2(1):16.
35. Santana L, Lino Alves J, da Costa Sabino Netto A. A study of parametric calibration for low cost 3D printing: Seeking improvement in dimensional quality. Materials & Design. 2017;135:159-72.
36. Wittbrodt B, Pearce JM. The effects of PLA color on material properties of 3-D printed components. Additive Manufacturing. 2015;8:110-6.
37. Wu W, Geng P, Li G, Zhao D, Zhang H, Zhao J. Influence of Layer Thickness and Raster Angle on the Mechanical Properties of 3D-Printed PEEK and a Comparative Mechanical Study between PEEK and ABS. Materials (Basel, Switzerland). 2015;8(9):5834-46.
38. Farah S, Anderson DG, Langer R. Physical and mechanical properties of PLA, and their functions in widespread applications — A comprehensive review. Advanced Drug Delivery Reviews. 2016;107(Supplement C):367-92.
39. Compressive Strength Testing of Plastics [Internet]. Available from: http://www.matweb.com/reference/compressivestrength.aspx.

40. Rodríguez JF, Thomas JP, Renaud JE. Mechanical behavior of acrylonitrile butadiene styrene (ABS) fused deposition materials. Experimental investigation. Rapid Prototyping Journal. 2001;7(3):148-58.
41. McLouth TD, Severino JV, Adams PM, Patel DN, Zaldivar RJ. The impact of print orientation and raster pattern on fracture toughness in additively manufactured ABS. Additive Manufacturing. 2017;18:103-9.
42. Chacon JM, Caminero MA, Garcia-Plaza E, Nunez PJ. Additive manufacturing of PLA structures using fused deposition modelling: Effect of process parameters on mechanical properties and their optimal selection. Materials & Design. 2017;124:143-57.
43. Lakatos É, Magyar L, Bojtár I. Material Properties of the Mandibular Trabecular Bone. Journal of Medical Engineering. 2014;2014:7.
44. Goldstein SA. The mechanical properties of trabecular bone: Dependence on anatomic location and function. Journal of Biomechanics. 1987;20(11):1055-61.
45. Oftadeh R, Perez-Viloria M, Villa-Camacho JC, Vaziri A, Nazarian A. Biomechanics and mechanobiology of trabecular bone: a review. Journal of biomechanical engineering. 2015;137(1).
46. Zhou B, Liu XS, Wang J, Lu XL, Fields AJ, Guo XE. Dependence of Mechanical Properties of Trabecular Bone on Plate-Rod Microstructure Determined by Individual Trabecula Segmentation (ITS). Journal of biomechanics. 2014;47(3):702-8.
47. Choi J, Kim S, Shin D-A. Biomechanical Comparison of Spinal Fusion Methods Using Interspinous Process Compressor and Pedicle Screw Fixation System Based on Finite Element Method. Journal of Korean Neurosurgical Society. 2016;59(2):91-7.

Conceptualization	Ideas; formulation or evolution of overarching research goals and aims By Elena Provaggi, Claudio Capelli, Deepak M. Kalaskar
Methodology	Development or design of methodology; creation of models By Elena Provaggi , Claudio Capelli , Deepak M. Kalaskar
Validation	Verification, whether as a part of the activity or separate, of the overall replication/ reproducibility of results/experiments and other research outputs By Elena Provaggi , Claudio Capelli , Benyamin Rahmani , Gaetano Burriesci, Deepak M. Kalaskar
Formal Analysis	Application of statistical, mathematical, computational, or other formal techniques to analyze or synthesize study data By Elena Provaggi , Claudio Capelli , Benyamin Rahmani
Investigation	Conducting a research and investigation process, specifically performing the experiments, or data/evidence collection By Elena Provaggi
Resources	Provision of study materials, reagents, materials, patients, laboratory samples, animals, instrumentation, computing resources, or other analysis tools By Claudio Capelli, Gaetano Burriesci , Deepak M. Kalaskar
Data Curation	Management activities to annotate (produce metadata), scrub data and maintain research data (including software code, where it is necessary for interpreting the data itself) for initial use and later reuse By Deepak M. Kalaskar
Writing – Original Draft	Preparation, creation and/or presentation of the published work, specifically writing the initial draft (including substantive translation) By Elena Provaggi
Writing – Review & Editing	Preparation, creation and/or presentation of the published work by those from the original research group, specifically critical review, commentary or revision – including pre-or postpublication stages By Elena Provaggi , Claudio Capelli , Benyamin Rahmani , Gaetano Burriesci, Deepak M. Kalaskar
Visualization	Preparation, creation and/or presentation of the published work, specifically visualization/ data presentation By Elena Provaggi
Supervision	Oversight and leadership responsibility for the research activity planning and execution, including mentorship external to the core team By Claudio Capelli , Benyamin Rahmani , Gaetano Burriesci, Deepak M. Kalaskar
Project	Management and coordination responsibility for the research activity planning and

Administration	execution By Deepak M. Kalaskar
Funding Acquisition	Acquisition of the financial support for the project leading to this publication Deepak M. Kalaskar